ARTICLE
Electrochemical Materials and Technologies

eISSN: 2949-0561

Cite this: Electrochem. Mater. Technol. 3 (2024) 20243033

Received: 25 March 2024
Accepted: 4 May 2024

DOI: 10.15826/elmattech.2024.3.033

Facile preparation of a PbS:Ni nanostructure using solid state synthesis route: microstructural, dielectric, and electrical properties

Amir Sultan [a, b], Mushtaq Ahmad [b *], Muhammad Zubair Khan [c], Junaid ur Rehman [d], Zahid Imran [b], Muhammad Bilal Hanif [e *], Martin Motola [e *]

In the present study, a novel PbS:Ni (10 at. %) nanostructure was synthesised via a simple solid state reaction method at 400 °C and constant pressure. X-ray diffraction analysis confirms the formation of a face-centred cubic crystalline structure. Preferential growth is observed along the (311) plane direction. The calculated crystallite size of PbS:Ni (10 at. %) from XRD analysis was found to be equal to 65 nm. Scanning electron microscopy revealed the formation of nanostructured PbS:Ni (10 at. %) materials. Its band gap of ~ 2.14 eV was determined by photoluminescence spectroscopy. Raman spectroscopy was used to confirm the structure of the material. Electrical properties were studied by I-V characteristic at ± 5 V and a temperature range from 100 K to 300 K. The ln V-ln I plot showed a non-linear behaviour of PbS:Ni (10 at. %). Impedance spectroscopy is applied at temperatures from 100 K to 300 K in a frequency range from 20 Hz to 2 MHz to observe the dielectric response of PbS:Ni (10 at. %). As obtained, $\varepsilon' \sim 26$ and conductivity in the order of 10^{-4} S · cm^{-1} were obtained at all temperatures above 10^4 Hz. The results obtained from photoluminescence spectroscopy, I-V characteristics and impedance spectroscopy confirm that PbS:Ni (10 at. %) can be considered as a suitable material for optoelectronic applications.

keywords: PbS, Ni, solid-state reaction, photoluminescence spectroscopy, impedance spectroscopy, dielectric

1. Introduction

Lead sulphide (PbS) is an important member of the metal sulphide family. PbS has a cubic crystal structure and, as an A_4B_6 semiconductor material, has a narrow direct bandgap of 0.41 eV [1]. PbS is therefore used as an infrared sensor [2]. In addition, it contains an intrinsically large excitation Bohr radius, i.e. 18 nm [3], and is nowadays used in a wide range of applications such as inductive photo resistors, optoelectronic devices, infrared detectors, solar cells [4], photography [5], solar radiation absorption [6], optical switching devices, diode lasers, temperature sensors, LEDs, solar control, humidity and decorative coatings [7–9]. To achieve the appropriate physical properties of PbS, which are critical for the above applications, PbS is often doped with metals. The concentration and type of dopant are responsible for changing the efficiencies and physical properties of PbS. Various doping techniques, i.e., chemical bath deposition [10–14], spray pyrolysis [15], successive ionic layer adsorption and reaction, electrodeposition [16, 17], microwave heating [18, 19], vacuum evaporation [20], microwave irradiation methods, hydrothermal synthesis, co-precipitation method, sonochemical routes, solid-state reaction route and self-propagating high temperature method [21, 22] are used for PbS doping.

In general, after metal doping of PbS, the band gap increases while the particle size decreases. This makes PbS

---

a: Jerzy Haber Institute of Catalysis and Surface Chemistry, Polish Academy of Sciences, Niezapominajek 8, Krakow PL-30239, Poland
b: Department of Physics, COMSATS University Islamabad (CUI), Park Road, Islamabad 45550, Pakistan
c: Department of Materials Science and Engineering, Pak-Austria Fachhochschule: Institute of Applied Sciences and Technology, Mang, Haripur, Khyber Pakhtunkhwa 22601, Pakistan
d: Materials Science Engineering and Commercialization (MSEC), Texas State University, San Marcos TX-78666, USA.
e: Department of Inorganic Chemistry, Faculty of Natural Sciences, Comenius University in Bratislava, Bratislava 842 15, Slovakia
* Corresponding authors: M. Ahmad (mushtaq.a@comsats.edu.pk), M.B. Hanif (bilalhanif46@gmail.com; hanifl@uniba.sk), M. Motola (martin.motola@uniba.sk)

suitable for optoelectronic applications such as LEDs, photography, IR detectors and solar cells [23, 24]. Among the variety of techniques, the simple solid-state reaction is often used for metal doping of PbS due to its potential for industrial scalability. It is essential to acknowledge that its perceived advantage in cost-effectiveness may not always hold true, primarily due to the extended synthesis times involved. However, the primary rationale behind the widespread use of solid-state synthesis lies in its capacity for industrial scaling. This method facilitates the production of PbS derivatives in bulk quantities, meeting the demands of large-scale applications across industries. Therefore, while other synthesis methods may offer distinct advantages based on different criteria, the solid-state reaction method remains a cornerstone in the fabrication of PbS-based materials, particularly due to its potential for efficient and scalable production [54, 55].

Shkir et al. [56–60] have made significant progress in the field of optoelectronic materials by synthesizing and characterizing a diverse array of PbS-based nanostructures tailored for various applications. In their pioneering work, they crafted Bi@PbS nanosheets [56], elucidating the unique structural and morphological attributes of these hybrid nanostructures. Additionally, their exploration into Ag-doped PbS nanoparticles [57] shed light on the intricate interplay between dopant concentration and material properties, offering valuable insights for optimizing optoelectronic device performance.

Moreover, Shkir et al. explored the fabrication of PbS microflowers [58], shedding light on the impact of morphology on light-matter interactions and device functionality. Their investigation into Pt-doped PbS nanopowders [59] further expanded the horizon of possibilities, demonstrating the tunability of optical and electrical characteristics through controlled doping strategies. Furthermore, their synthesis of PbS nanosheets [60] provided comprehensive insights into the structural, morphological, and optoelectronic properties of these nanostructures, paving the way for advancements in device design and fabrication.

We have already worked on PbS nanostructure where we doped 1 at. % and 3 at. % Ni in PbS at a sintering temperature of 400 °C and studied their dielectric properties in the temperature range of 198 K to 358 K [25]. We continue to work on PbS nanostructure and in this work a solid-state reaction route was used to prepare a Ni-heavy PbS derivative at a sintering temperature of 400 °C. After the successful synthesis then we analysed and studied the effect of 10 at. % Ni doping in PbS by using several characterisation techniques including scanning electron microscopy (SEM), X-ray diffraction (XRD), photoluminescence (PL), Raman spectroscopy, *I*–*V* characteristics and electrochemical impedance spectroscopy (EIS) were carried out.

2. Experimental

2.1. Materials and synthesis method

A solid-state reaction route was used for the synthesis and doping of Ni in PbS. The basic precursors were purchased from Sigma Aldrich and used without further purification. The stoichiometric amounts of the corresponding precursors of nickel (Ni), lead (Pb) and sulphur (S), i.e, Lead acetate trihydrate [$Pb(CH_3COO)_2 \cdot 3H_2O$; 99 %] for lead (Pb), thiourea [$SC(NH_2)_2$; ≥ 99.0 %] for sulphur (S) and nickel acetate tetrahydrate [$Ni(CH_3COO)_2 \cdot 4H_2O$; 99.9 %] for nickel (Ni) were taken, simply mixed and these precursors were ground in a mortar and pestle for 1 hour for the fine mixture. After grinding, the mixed powder was placed in an air furnace at 400 °C for 5 hours to anneal the ground sample and evaporate the excess precursors. After annealing, the samples were ground again for 10 minutes to obtain the fine powder. For further characterisation, the final product was obtained in the form of black powder. The chemical reaction that takes place for the formation of Ni-doped PbS during the solid-state reaction route. H_2S reacts with Pb^{2+} ions to form PbS which reacts with Ni^{2+} ions to form PbS: Ni where Ni^{2+} ions substituted into Pb^{2+} ions in host PbS.

The imaginable chemical reactions during PbS formation are explained as follows. First, the decomposition of thiourea occurs at temperature 150 °C [21] as given in Equation (1–4).

$$SC(NH_2)_2 \xrightarrow{\sim 150°C} NH_2CN + H_2S, \tag{1}$$

Then H_2S reacts with lead decomposed from lead acetate to form black-colored PbS as shown

$$PbS^{2+} + H_2S \rightarrow PbS + 2H^+, \tag{2}$$

A similar procedure was adopted to prepare the doped PbS with Ni in 10 % atomic weight ratio. The general form of the doped sample is written in the following form.

$$PbS + Ni = Pb_{1-x}Ni_xS, \tag{3}$$

In our case as the Ni is doped in 10 % so here $x = 0.1$. Then possible chemical form of material is written by the following formula.

$$PbS + Ni = Pb_{0.9}Ni_{0.1}S. \tag{4}$$

2.2. Characterization

Several characterization techniques were carried out on the finally obtained nano powders of PbS:Ni (10 at. %). For structural studies such as crystallite size (D), texture co-efficient (TC), *d*-spacing and lattice parameters of PbS:Ni (10 at. %), XRD (PANalytical X'Pert Pro) using CuKα radiation at 1.54 Å wavelength is used. A scanning electron microscope (JSM5910, JEOL, Japan) is used to study the surface morphology of PbS:Ni (10 at. %). Raman spectroscopy (Micro-Raman from Bruker and LabRam from Dongwoo Optron) is used to study the structure. The band gap of PbS:Ni (10 at. %) is calculated by photoluminescence (PL) spectroscopy (Dongwoo Optron's LabRam) using a 325 nm helium-cadmium laser. The *I-V* characteristic is used to study the electrical properties and impedance spectroscopy is used to study the dielectric response of PbS:Ni (10 at. %). The electrical equivalent circuit (EEC); (R_l, *CPE*) has been used to fit the impedance curves using the MINUIT library.

3. Results and discussion

The X-ray diffraction pattern in Figure 1a displays both pure PbS and PbS:Ni (10 at. %). In PbS:Ni (10 at. %), diffraction peaks were observed at 2θ positions of 25.94 °, 30.04 °, 43.02 °, 50.94 °, 53.36 °, 62.48 °, 68.82 °, 70.92 °, and 78.91 °, corresponding to the lattice planes (111), (200), (220), (311), (222), (400), (331), (420), and (422), respectively. Similarly, for pure PbS, diffraction peaks were detected at 2θ positions of 26.07 °, 30.17 °, 43.15 °, 51.05 °, 53.50 °, 62.62 °, 68.98 °, 70.92 °, and 78.91 °, corresponding to the same lattice planes. However, the lattice parameter for pure PbS and PbS:Ni (10 at. %) nanostructures at 2θ positions of 30.17 ° and 30.04 ° is 5.918 Å and 5.948 Å, respectively. This is in agreement with previous reports [26–30]. This XRD pattern of PbS:Ni (10 at. %) agrees well with a standard JCPDS card reference code of 00–005–0592, implying the formation of a face-centered cubic crystal structure. No impurity peaks of Ni are observed in the XRD pattern. This is due to the substitution of Ni^{2+} ions by Pb^{2+} ions at the regular site in the host PbS. Figure 1b shows the enlarged spectra of pure PbS and PbS:Ni (10 at. %). A clear diffraction shift to a lower 2θ diffraction angle was observed in the case of Ni-doping. This is due to internal stresses associated with the doping of Ni in PbS. The preferential growth is along the (311) plane direction, calculated using the texture coefficient formula given in Eq. (5):

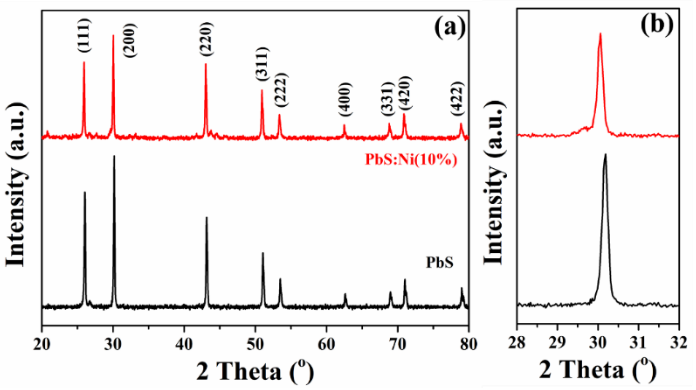

Figure 1 The XRD pattern of PbS:Ni (10 at. %) nanostructures (a). along with its magnified spectra (b).

$$TC_{(hkl)} = \frac{I_{(hkl)}/I_{r(hkl)}}{\frac{1}{n}\sum_n (I_{hkl}/I_{r(hkl)})}, \tag{5}$$

where $TC_{(hkl)}$ is the texture coefficient, $I_{(hkl)}$ is the intensities obtained from the XRD pattern, $I_{r(hkl)}$ is the intensities of the reference JCPDS card, and n is the number of diffractions.

The crystallite size and full-width half maximum (FWHM) values were calculated using the Scherrer equation (Eq. 6) and the average crystallite of ~ 65 nm was obtained.

$$D = \frac{K\lambda}{\beta Cos\theta}, \tag{6}$$

where D is crystallite size, K is constant, known as crystalline shape, $K = 0.94$ [30]. β is peak width, $\lambda = 1.540562$ Å wavelength of X-ray and θ is Bragg's diffraction angle.

Lattice constant (a) and *d*-spacing (d) were calculated using Eq. (7) (Bragg's law) and Equation (8) and the average lattice constant is 5.9429 Å which is in accordance with previous reports [29, 32].

$$2dsin\theta = n\lambda, \tag{7}$$

$$d = \frac{a}{\sqrt{h^2+k^2+l^2}}, \tag{8}$$

where d is the interplanar spacing, θ is the Braggs angle, λ is the wavelength of the x-ray source, *hkl* are miller indices, and a is the lattice constant.

Crystallite size, *d*-spacing, and lattice constant values are summarised in Table 1.

The scanning electron microscopy (SEM) was used to study the surface morphology of PbS:Ni (10 at. %). Figure 2a shows the SEM image of PbS:Ni (10 at. %), which clearly displays a porous network of agglomerated nanostructures in the form of grains with varying shapes and sizes that are loosely packed together. The formation of such agglomerates can be attributed to various factors,

Table 1 – Lattice constants, *d*-spacing and crystallite sizes of PbS:Ni (10 at. %).

Peak no.	2θ	(*hkl*)	*d* (Å)	*a* (Å)	D_{hkl} (nm)
1	25.94 °	(111)	3.4346	5.9489	57
2	30.04 °	(200)	2.9744	5.9488	58
3	43.02 °	(220)	2.1026	5.9471	72
4	50.94 °	(311)	1.7912	5.9407	76
5	53.36 °	(222)	1.7155	5.9427	62
6	62.48 °	(400)	1.4852	5.9408	81
7	68.82 °	(331)	1.3630	5.9412	56
8	70.92 °	(420)	1.3277	5.9376	68
9	78.90 °	(422)	1.2122	5.9385	60

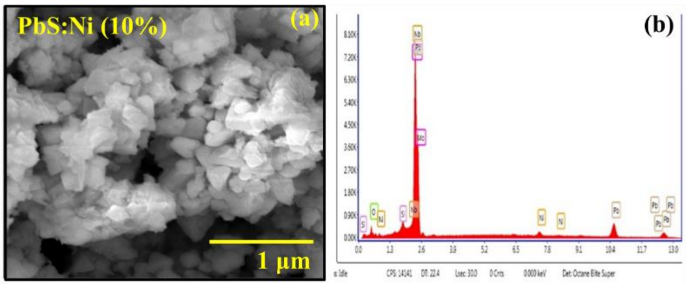

Figure 2 SEM image of PbS:Ni (10 at. %) nanostructures (a). EDS graph of PbS:Ni (10 at. %) nanostructures (b).

including the synthesis conditions, precursor characteristics, and aggregation kinetics. In our synthesis method, the solid-state reaction route at a sintering temperature of 400 °C may have facilitated the formation of these agglomerates due to the coalescence of nanoparticles during the annealing process. Additionally, factors such as surface energy minimization and particle-particle interactions can promote the aggregation of nanoparticles into larger structures. The detailed composition is explained in experimental section. The doping was performed in PbS with 10 % of Ni therefore the chemical composition of prepared sample is $Pb_{0.9}Ni_{0.1}S$.

Additionally, Figure 2b presents the EDS graph of PbS:Ni (10 at. %), indicating the presence of Ni in PbS.

The bandgap energy of PbS:Ni (10 at. %) was determined using photoluminescence (PL) spectroscopy. The PL spectrum of PbS:Ni (10 at. %) exhibits an emission peak at λ = 578 nm, as shown in Figure 3. The calculated bandgap value of PbS:Ni (10 at. %) is 2.14 eV. Comparison with the previous results [25] shows that the band gap of PbS:Ni (10 at. %) sintered at 400 °C has increased slightly.

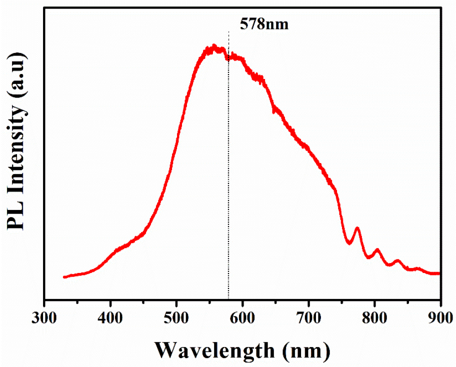

Figure 3 Shows the PL spectrum of PbS:Ni (10 at. %) nanostructures at room temperature.

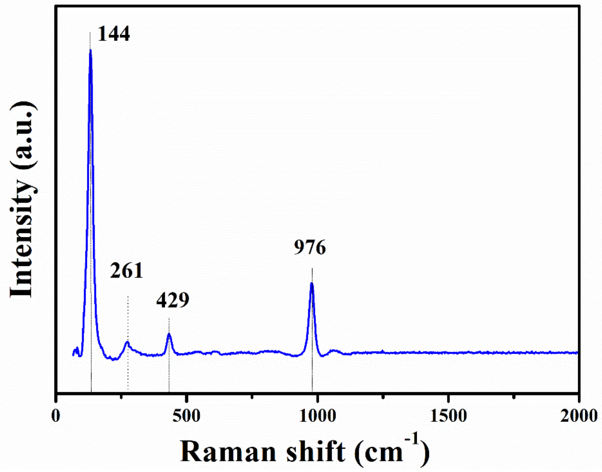

Figure 4 Raman spectrum of PbS:Ni (10 at. %) nanoparticles at room temperature.

Figure 4 displays the Raman spectrum of PbS:Ni (10 at. %) nanostructures at room temperature. Prominent bands are observed at approximately 144, 261, 429, and 976 cm^{-1}. The band at 144 cm^{-1} is due to the combination of transverse and longitudinal acoustic phonon modes in the PbS:Ni. This band is assigned to the scattering of two constant wave number phonons in the Brillouin zone in the PbS:Ni crystal structure. Ni crystal structure. The band at 261 cm^{-1} corresponds to PbO. No diffraction of PbO was observed in the XRD analysis (Figure 1). Therefore, the formation of PbO is attributed to photo-degradation, as indicated by Raman spectroscopy. The band at 429 cm^{-1} corresponds to the first overtone of longitudinal optical (LO) phonon in the center of the Brillouin zone, while the band at 976 cm^{-1} is attributed to oxides-sulfates [33, 34].

The *I*-*V* characteristics describe the electric current response of the prepared material to an applied voltage or field. *I*-*V* measurements were performed on a pressed pellet of PbS:Ni (10 at. %) at temperatures ranging from 100 K to 300 K, with an applied voltage varying from –5 V to +5 V. The *I*-*V* curves are influenced by several factors, including the material, applied electric field, temperature, doping type, and doping concentration. The direction of the current along the *x* and *y* axes determines whether the material is under reverse or forward bias. To observe the conduction mechanism, we plot the In-In values of current and voltage, following the power equation $I \propto V^m$. The type of conduction mechanism can be determined by the slope m of the curve in the ln-ln graph. If the slope is around 1, then it is ohmic, indicating metallic behaviour of the prepared material. If the slope is between 1 and 2, the conduction mechanism is either Poole Frankel or Schottky. If the slope is around 2, the conduction mechanism would be space charge limited current (SCLC) [35]. Figure 5a displays the non-linear (non-ohmic) *I*-*V* characteristic curve, and Figure 5b shows the ln *V*-ln *I* plot of PbS:Ni (10 at. %). The current changes with temperature, confirming the semiconductor behaviour of PbS:Ni (10 at. %). The slope was calculated using the power equation, resulting in a value of 1.401. This indicates that PbS:Ni (10 at. %) displays Schottky behaviour.

Impedance spectroscopy was used to evaluate the dielectric response of PbS:Ni (10 at. %) at temperatures ranging from 100 K to 300 K (in 20 K increments) in a pressed pellet. The thickness and dimeter of the pellet is 1.69 mm and 13.15 mm respectively and silver electrode was paste on the pellet during the impedance spectroscopy measurement. The AC voltage was applied at an amplitude of 1 V and a frequency range of 20 Hz to 2 MHz was used.

Figure 6 displays the relationship between frequency and conductivity variation of PbS:Ni (10 at. %). It is evident that the conductivity is temperature-dependent. The conductivity values at 100 K and 300 K and 2 MHz were 2.52 · 10⁻⁴ S · m⁻¹ and 3.01 · 10⁻⁴ S · m⁻¹, respectively. The frequency versus conductivity graph comprises two sections. The first section is independent of frequency but dependent on temperature, i.e., the conductivity remains constant with frequency (i.e., DC conductivity). The section of the frequency vs conductivity graph that is dependent on frequency and temperature is known as AC conductivity. The frequency at which the conductivity experiences a sharp increase is referred to as the hopping frequency. The conductivity is composed of two parts: real and imaginary. The real part of the conductivity was calculated using Eq. 9 [36].

$$\sigma'_{ac} = \left(\frac{Z'}{Z'^2+Z''^2}\right)\frac{d}{A}, \tag{9}$$

where Z' and Z'' are the real and imaginary parts of the impedance, A and d are the area and thickness of the pellet, respectively. The real part of conductivity consists of two parts as discussed above, i.e., DC and AC conductivity [37].

$$\sigma'_{ac} = \sigma_1(T) + \sigma_2(\omega, T), \tag{10}$$

where $\sigma_1(T)$ and $\sigma_2(\omega, T)$ are dc and ac conductivity respectively.

$$\sigma_1(T) = \sigma_0 \exp\left(-\frac{E_a}{K_B T}\right), \tag{11}$$

and,

$$\sigma_2(\omega, T) = B(T)\omega^s(T), \tag{12}$$

where E_a is activation energy, K_B is Boltzmann constant, σ_0 pre-exponential factor, s dimensionless constant and $B(T)$ is temperature-dependent parameter having unit of conductivity.

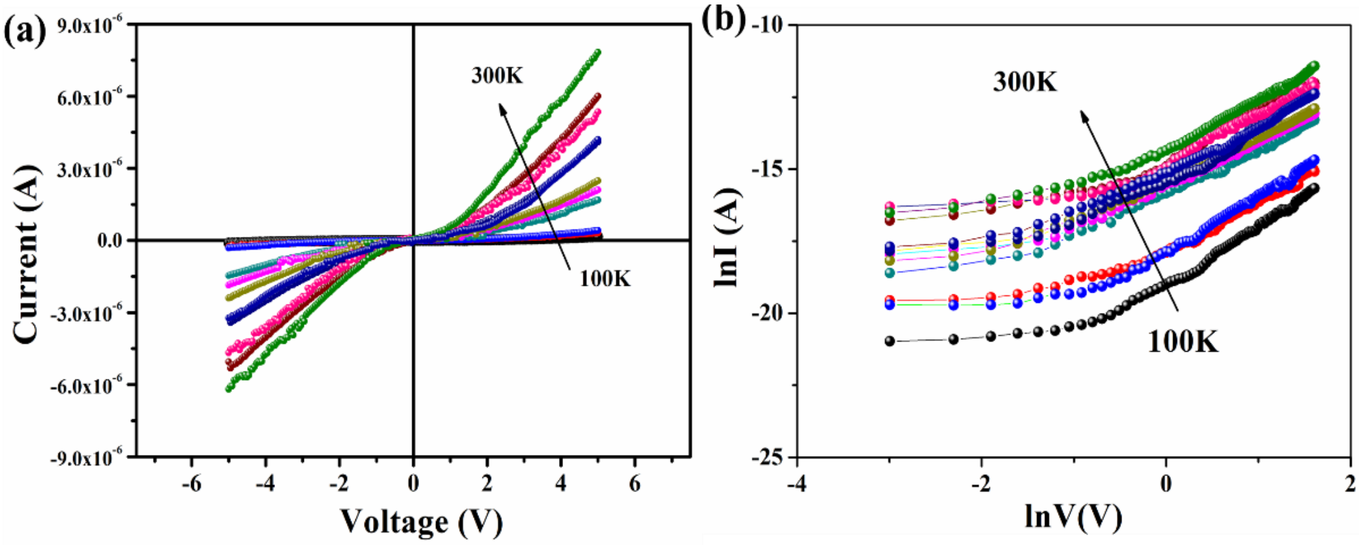

Figure 5 Temperature-dependent *I*-*V* curve (a) and temperature-dependent ln *V*-ln *I* curve (b) of PbS:Ni (10 at. %).

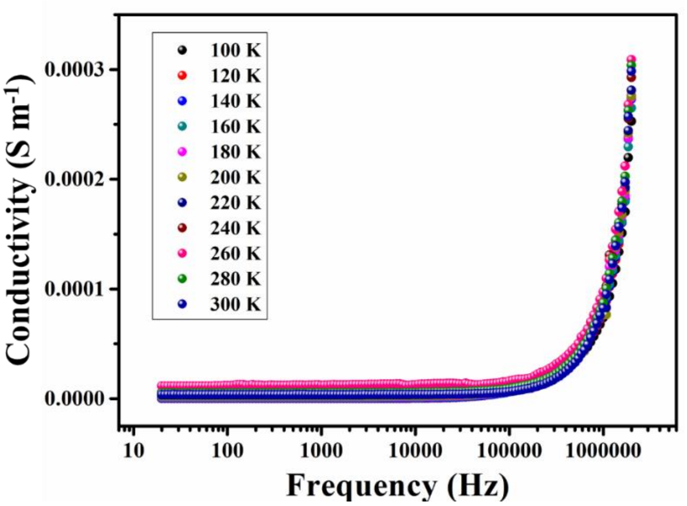

Figure 6 Frequency *vs* conductivity variation of PbS:Ni (10 at. %).

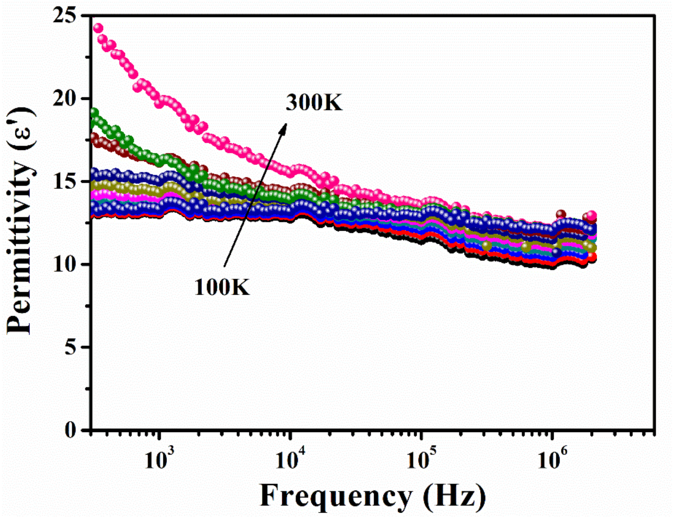

Figure 7 Frequency *vs* real part of permittivity (ε') of PbS:Ni (10 at. %).

Figure 7 shows the frequency vs permittivity (real part) of PbS:Ni (10 at. %) at different temperatures and frequencies. The permittivity values are observed to be high at lower frequencies and decrease with an increase in frequency. At high frequencies, the permittivity values become independent of frequency. The reduction in permittivity values at higher frequencies is due to polarization, which cannot fully align itself during a frequency cycle in the available time.

At lower frequencies, the higher permittivity is a result of the integrated effect of atomic, interfacial, ionic, and electronic polarizations [37–39]. When the measuring frequency is overcome by the relaxation frequency, every type of polarization affects the permittivity. Therefore, the interfacial polarization characteristic to grain boundaries at lower frequencies causes larger values of permittivity. Maxwell – Wagner's theory explains the variation in permittivity with frequency, which is in good agreement with Koop's phenomenological theory. According to Maxwell – Wagner theory, the interfacial polarization characteristic of the grain boundary is prominent at lower frequencies because the grain boundary behaves like a barrier to the flow of charge carriers [40, 41].

The reason for high permittivity values at lower frequencies can be explained as follows: PbS:Ni nanoparticles contain a large number of disordered ions, including positive ions of lead and nickel and negative ions of sulphur vacancies. These ions behave like shallow acceptors at grain boundaries [42]. Ni nanoparticles consist of a large number of disordered ions, including positive ions of lead and nickel and negative ions of sulphur vacancies. When an external electric field is applied, the dipole moments within the material rotate in response. These rotated dipole moments, which are due to externally applied fields at grain boundaries, contribute to the permittivity of PbS:Ni. Additionally, the grain boundaries of dense nanomaterials at high pressure contain numerous defects, such as vacancies, dangling bonds, and porosities, which cause changes in the positive and negative space charge distributions [42]. When an external electric field is applied, positive and negative ions move towards the positive and negative poles of the field, respectively. At the same time, a large number of dipole moments are inevitably created after being trapped by the defects [43]. The high permittivity values for PbS:Ni (10 at. %) nanostructures are caused by the space charge polarization at grain boundaries. For temperatures above 104 Hz, we obtained ε' of approximately 26, which is higher than that of the bulb PbS, which is about 17.

Figure 8 displays the frequency versus the real and imaginary parts of PbS:Ni (10 at. %). In both figures, Z' and Z'' are temperature-dependent, meaning that their values change with temperature. A phenomenon known as negative temperature coefficient of resistance was observed, resulting in a decrease in the values of Z' and Z'' with increasing temperature, indicating an increase in conduction. Furthermore, the values of Z' and Z'' decrease with increasing frequency. At higher frequencies, these values tend to merge for all temperatures, indicating the possible release of space charges [44]. At lower frequencies, they interact with interfaces and grain boundaries, whereas at higher frequencies, they interact with the bulk of the material. The bulk is more conductive than interfaces and grain boundaries. The frequency *vs* Z'' spectrum provides information about the system relaxation time.

Figure 9a displays the Nyquist plot of PbS:Ni (10 at. %), depicting Z' *vs* Z'' where Z' and Z'' represent the real and imaginary parts of impedance, respectively. The plot illustrates an increasing frequency from right to left and is used to identify the most resistive parts, such as grain boundaries and sub-grain boundaries, in the structure [45]. The Nyquist plot comprises one or more semi-circular arcs that provide information about the relaxation processes. The arc at lower frequencies suggests a grain boundary effect, while the arc at higher frequencies is consistent with a bulk effect. The Nyquist plot indicates a semi-circular arc at all temperatures, which is centred in the high frequency region [46]. Additionally, the diameter of the semi-circular arc is larger at lower temperatures i.e. at 100 K, indicating higher impedance that decreases with increasing temperatures. At high temperatures, the impedance of semiconductor materials decreases due to the thermal activation of charge carriers.

Figure 9b displays the activation energy of Ni-doped PbS (10 at. %), which was found to be 0.10 eV. It has been reported in the literature that the activation energy of pure PbS is approximately 0.22 eV [45]. The decrease in activation energy of Ni-doped PbS may be attributed to the creation of interstitial levels by the doped material and higher ionization energies caused by oxygen vacancies.

To enhance comprehension, we compared the band gap and dielectric value of PbS:Ni (10 at. %) with the literature values, as presented in Table 2.

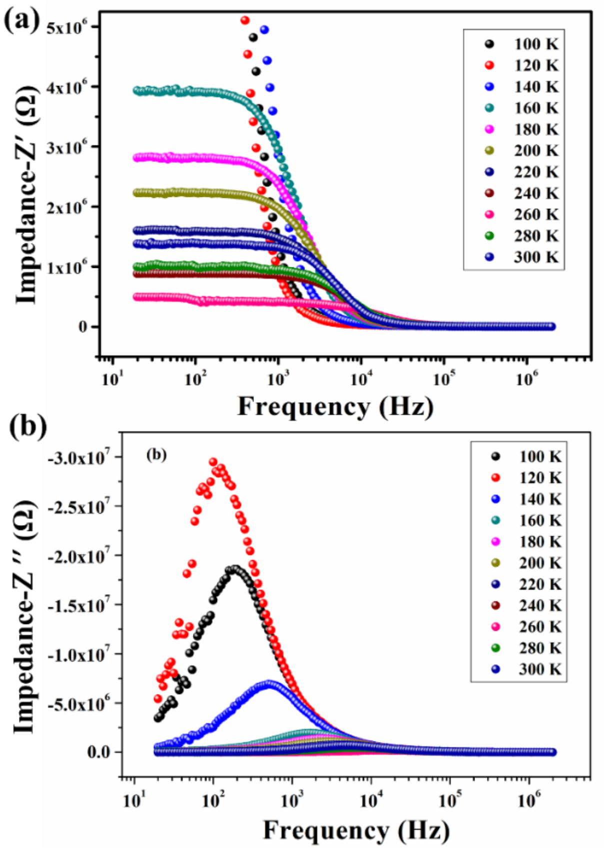

Figure 8 Frequency *vs* real part Z' (a) and imaginary part Z'' (b) of impedance spectra.

Table 2 – Comparison of Band gap and Dielectric constant values of PbS:Ni (10 at. %) with literature.

Materials	Synthesis route	Band gap	Dielectric constant	Ref.
Zn-doped PbS film	Chemical bath deposition technique	1.39 eV	–	[47]
Nanocrystalline PbS thin films	Thin film coating	2.40 eV	–	[48]
PbS quantum dots	*ab initio* method	1.49 eV	–	[49]
PbS nanoparticles	Inflight sintering	2.00 eV	–	[50]
PbS–PVA nanocomposite thin films	Chemical bath deposition	2.50 eV	155	[51]
Ce doped PbS NPs	Low-cost chemical route	3.04 eV	24.5	[52]
Y-doped PbS NPs	Coprecipitation chemical synthesis	1.37 eV	28	[53]
Ni-doped PbS NPs	Coprecipitation	1.89 eV	–	[30]
Ni-doped PbS nanostructure	Solid state route	2.14 eV	26	This study

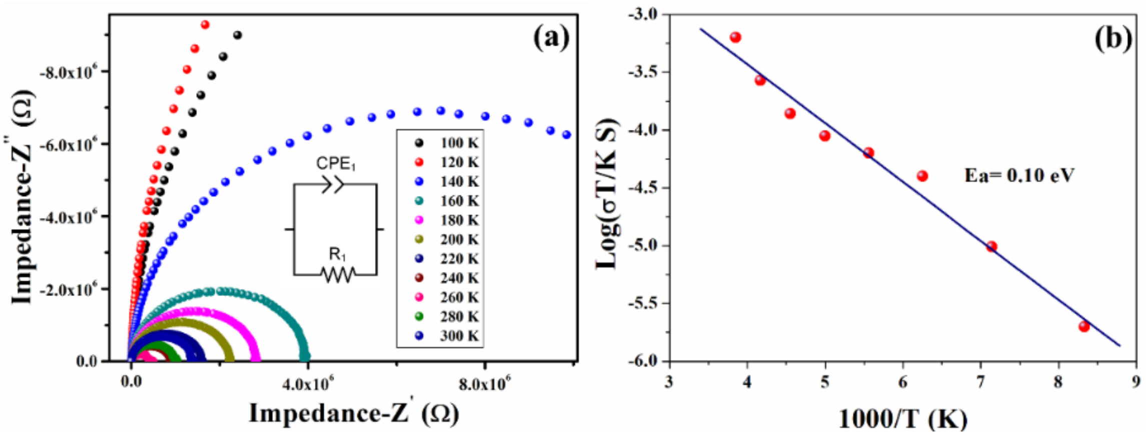

Figure 9 Nyquist plot (Z' *vs* Z''), inset is the equivalent circuit (a) and the activation energy of PbS:Ni (10 at. %) (b).

4. Conclusions

PbS:Ni (10 at. %) nanostructures were synthesized using a solid-state reaction method at atmospheric pressure and 300 °C. X-ray diffraction and scanning electron microscopy confirmed the face-centered cubic crystalline phase nanostructure with a crystallite size of approximately 65 nm. The preferential growth of PbS:Ni (10 at. %) was observed along the (311) plane direction. The photoluminescence spectroscopy calculation yielded an optical band gap of 2.14 eV. The *I*-*V* characteristic indicates non-ohmic behavior of PbS:Ni (10 at. %). Impedance spectroscopy was conducted on PbS:Ni (10 at. %) nanostructures at a temperature range of 100–300 K and frequencies ranging from 20 Hz to 2 MHz. The results showed good permittivity and conductivity values compared to pure PbS. Therefore, it can be concluded that PbS:Ni (10 at. %) synthesized at 400 °C is a suitable candidate for optoelectronic applications.

Supplementary materials

No supplementary materials are available.

Funding

Grant of the Comenius University Bratislava for Young Scientists (UK/3/2022). This study was supported by the Operation Program of Integrated Infrastructure for the project, UpScale of Comenius University Capacities and Competence in Research, Development and Innovation, ITMS2014+: 313021BUZ3, co-financed by the European Regional Development Fund. The research leading to these results was funded in part by the statutory research fund of Jerzy Haber Institute of Catalysis and Surface Chemistry Polish Academy of Sciences ICSC PAS.

Acknowledgments

None.

Author contributions

Amir Sultan: Formal Analysis; Investigation; Resources; Software; Validation.

Zahid Imran: Formal Analysis; Investigation; Resources.

Kashif Khan: Formal Analysis; Investigation; Methodology.

Mushtaq Ahmad: Resources; Investigation; Software.

Junaid ur Rehman: Formal Analysis; Investigation; Methodology.

Muhammad Bilal Hanif: Visualization; Validation; Methodology; Writing – Original draft; Writing – Review & Editing.

Martin Motola: Conceptualization; Validation; Data curation; Funding acquisition; Writing – Original draft; Writing – Review & Editing; Project administration; Supervision.

Conflict of interest

The authors declare no conflict of interest.

Additional information

Scopus IDs:
Amir Sultan: AuthorId=58107876500.
Muhammad Bilal Hanif: AuthorId=57212407701.
Martin Motola: AuthorId=57197866926.

References

1. Rajashree C, Balu AR, Nagarethinam VS, Properties of cd doped PbS thin films: doping concentration effect, Surf. Eng., **31(4)** (2015) 316. https://doi.org/10.1179/1743294415Y.0000000014

2. Liu X, Zhang M, Studies on PbS and PbSe detectors for IR System, Int. J. Infrared Millim. Waves, **21** (2000) 1697–1701. https://doi.org/10.1023/A:1006676029014

3. Madelung O. III-V compounds, Semiconductors: Data Handbook. Publisher: Springer; 2004. P. 71–172.

4. RaviShankar S, Balu AR, Anbarasi M, Nagarethinam VS, Influence of precursor molar concentration on the structural, morphological, optical and electrical properties of PbS thin films deposited by spray pyrolysis technique using perfume atomizer, Optik, **126(20)** (2015) 2550–2555. https://doi.org/10.1016/j.ijleo.2015.06.039

5. Nair PK, Gomezdaza O, Nair MTS, Metal sulphide thin film photography with lead sulphide thin films, Adv. Mater. Opt. Electron., **1(3)** (1992) 139–145. https://doi.org/10.1002/amo.860010307

6. Akhtar S, Saeed N, Hanif MB, Dogar S, et al., PbS and PbO Thin films via e-beam evaporation: Morphology, structure, and electrical properties, Materials, **15(19)** (2022) 6884. https://doi.org/10.3390/ma15196884

7. Li D, Liang C, Liu Y, Qian S, Femtosecond nonlinear optical properities of PbS nanoparticles, J. Lumin., **122–123** (2007) 549–551. https://doi.org/10.1016/j.jlumin.2006.01.214

8. Gohar O, Khan MZ, Bibi I, Bashir N, et al., Nanomaterials for advanced energy applications: Recent advancements and future trends, Materials & Design, **241** (2024) 112930. https://doi.org/10.1016/j.matdes.2024.112930

9. Aryamol KS, Kanagaraj K, Nangan S, Haponiuk JT, et al., Recent Advances of carbon Pathways for Sustainable Environment development, Environmental Research, **250** (2024) 118513. https://doi.org/10.1016/j.envres.2024.118513

10. Naşcu C, Vomir V, Pop I, Ionescu V, et al., The study of lead sulphide films. VI. influence of oxidants on the chemically deposited PbS thin films, Mater. Sci. Eng.: B, **41(2)** (1996) 235–240. https://doi.org/10.1016/S0921-5107(96)01611-X

11. Larramendi EM, Calzadilla O, González-Arias A, Hernández E, et al., Effect of surface structure on photosensitivity in chemically deposited PbS thin films, Thin Solid Films, **389(1–2)** (2001) 301–306. https://doi.org/10.1016/S0040-6090(01)00815-X

12. Pentia E, Pintilie L, Tivarus C, Pintilie I, et al., Influence of Sb^{3+} ions on photoconductive properties of chemically deposited PbS films, Mater. Sci. Eng.: B, **80(1–3)** (2001) 23–26. https://doi.org/10.1016/S0921-5107(00)00578-X

13. Joshi RK, Kanjilal A, Sehgal HK, Solution grown PbS nanoparticle films, Appl. Surf. Sci., **221(1–4)** (2004) 43–47. https://doi.org/10.1016/S0169-4332(03)00955-3

14. Valenzuela-Jáuregui JJ, Ramírez-Bon R, Mendoza-Galván A, Sotelo-Lerma M, Optical properties of PbS thin films chemically deposited at different temperatures, Thin Solid Films, **441(1–2)** (2003) 104–110. https://doi.org/10.1016/S0040-6090(03)00908-8

15. Thangaraju B, Kaliannan P, Spray pyrolytically deposited PbS thin films, Semicond. Sci. Technol., **15** (2000) 849. https://doi.org/10.1088/0268-1242/15/8/311

16. Sharon M, Ramaiah KS, Kumar M, Neumann-Spallart M et al., Electrodeposition of lead sulphide in acidic medium, J. Electroanal. Chem., **436(1–2)** (1997) 49–52. https://doi.org/10.1016/S0022-0728(97)00124-1

17. Slonopas A, Alijabbari N, Saltonstall C, Globus T, et al., Chemically deposited nanocrystalline lead sulfide thin films with tunable properties for use in photovoltaics, Electrochimica Acta, **151** (2015) 140–149. https://doi.org/10.1016/j.electacta.2014.11.021

18. Ni Y, Wang F, Liu H, Yin G, et al., A novel aqueous-phase route to prepare flower-shaped PbS micron crystals, J. Cryst. Growth, **262(1–4)** (2004) 399–402. https://doi.org/10.1016/j.jcrysgro.2003.10.053

19. Zhao Y, Liao XH, Hong JM, Zhu JJ, Synthesis of lead sulfide nanocrystals via microwave and sonochemical methods, Mater. Chem. Phys., **87(1)** (2004) 149–153. https://doi.org/10.1016/j.matchemphys.2004.05.026

20. Springholz G, Bauer G, Investigation of $Pb_{1-x}Eu_xTe$ molecular beam epitaxy by reflection high-energy electron diffraction intensity oscillations, Appl. Phys. Lett., **60(13)** (1992) 1600. https://doi.org/10.1063/1.107238

21. Wang H, Zhang JR, Zhu JJ, Sonochemical preparation of lead sulfide nanocrystals in an oil-in-water microemulsion, J. Cryst. Growth, **246(1–2)** (2002) 161–168. https://doi.org/10.1016/S0022-0248(02)01808-0

22. Zhang W, Yang Q, Xu L, Yu W, et al., Growth of PbS crystals from nanocubes to eight-horn-shaped dendrites through a complex synthetic route, Mater. Lett., **59(27)** (2005) 3383–3388. https://doi.org/10.1016/j.matlet.2004.09.065

23. Nazir A, Toma A, Shah NA, Panaro S, et al., Effect of ag doping on opto-electrical properties of CdS thin films for solar cell applications, J. Alloys Compd., **609** (2014) 40–45. https://doi.org/10.1016/j.jallcom.2014.04.144

24. Kaci S, Keffous A, Hakoum S, Mansri A, Hydrogen sensitivity of the sensors based on nanostructured lead sulfide thin films deposited on a-SiC:H and p-Si(100) substrates, Vacuum, **116** (2015) 27–30. https://doi.org/10.1016/j.vacuum.2015.02.024

25. Sultan A, Ahmad M, Imran Z, Batool SS, et al., Tailoring structural, dielectric and optical effects of PbS nanosheets with ni doping, Phys. B: Condens. Matter, **602** (2021) 412571. https://doi.org/10.1016/j.physb.2020.412571

26. Hussain A, Begum A, Rahman A, Electrical and optical properties of nanocrystalline lead sulphide thin films prepared by chemical bath deposition, Indian J. Phys., **86** (2012) 697–701. https://doi.org/10.1007/s12648-012-0130-2

27. Rajashree C, Balu AR, Tuning the physical properties of PbS thin films towards optoelectronic applications through Ni doping, Optik, **127(20)** (2016) 8892–8898. https://doi.org/10.1016/j.ijleo.2016.06.106

28. Garcia OP, Albuquerque MCC, Aquino KAS, Araujo PLB, et al., Use of lead (II) sulfide Nanoparticles as stabilizer for PMMA exposed to gamma Irradiation, Mater. Res., **18(2)** (2015) 365. https://doi.org/10.1590/1516-1439.330214

29. Navaneethan M, Nisha KD, Ponnusamy S, Muthamizhchelvan C, Optical and surface morphological properties of triethylamine passivated lead sulphide nanoparticles, Mater. Chem. Phys., **117(2–3)** (2009) 443–447. https://doi.org/10.1016/j.matchemphys.2009.06.026

30. Parveen A, Agrawal S, Azam A, Band gap tuning and fluorescence properties of lead sulfide $Pb_{0.9}A_{0.1}S$ (A: Fe, Co, and Ni) nanoparticles by transition metal doping, Opt. Mater., **76** (2018) 21–27. https://doi.org/10.1016/j.optmat.2017.12.015

31. Langford JI, Wilson AJC, Scherrer after sixty years: A survey and some new results in the determination of crystallite size, J. Appl. Crystallogr., **11** (1978) 102–113. https://doi.org/10.1107/S0021889878012844

32. Rajashree C, Balu AR, Nagarethinam VS, Properties of cd doped PbS thin films: doping concentration effect, Surf. Eng., **31(4)** (2015) 316. https://doi.org/10.1179/1743294415Y.0000000014

33. Priyanka U, Akshay Gowda KM, Elisha MG, Surya Teja B, et al., Biologically synthesized PbS nanoparticles for the detection of arsenic in water, Int. Biodeterior. & Biodegradation, **119** (2017) 78–86. https://doi.org/10.1016/j.ibiod.2016.10.009

34. Smith GD, Firth S, Clark RJH, Cardona M, First- and second-order Raman spectra of galena (PbS), J. Appl. Phys., **92(8)** (2002) 4375–4380. https://doi.org/10.1063/1.1505670

35. Shapter JG, Brooker MH, Skinner WM, Observation of the oxidation of galena using Raman spectroscopy, Int. J. Miner. Process., **60(3–4)** (2000) 199–211. https://doi.org/10.1016/S0301-7516(00)00017-X

36. Chiu FC, A review on conduction Mechanisms in dielectric Films, Adv. Mater. Sci. Eng., **2014** (2014) 1. https://doi.org/10.1155/2014/578168

37. Ahmad M, Rafiq MA, Hasan MM, Transport characteristics and colossal dielectric response of cadmium sulfide nanoparticles, J. Appl. Phys., **114** (2013) 133702. https://doi.org/10.1063/1.4823810

38. Afsar MF, Jamil A, Rafiq MA, Ferroelectric, dielectric and electrical behavior of two-dimensional lead sulphide nanosheets, Adv. Nat. Sci.: Nanosci. Nanotechnol., **8** (2017) 045010. https://doi.org/10.1088/2043-6254/aa8b3d

39. Rasool K, Rafiq MA, Li CB, Krali E, et al., Enhanced electrical and dielectric properties of polymer covered silicon nanowire arrays, Appl. Phys. Lett., **101** (2012) 023114. https://doi.org/10.1063/1.4735278

40. Batoo KM, Kumar S, Lee CG, Alimuddin, Finite size effect and influence of temperature on electrical properties of

nanocrystalline Ni–Cd ferrites, Curr. Appl. Phys., **9(5)** (2009) 1072–1078. https://doi.org/10.1016/j.cap.2008.12.002

41. Sathishkumar G, Venkataraju C, Sivakumar K, Synthesis, structural and dielectric Studies of nickel Substituted Cobalt-Zinc Ferrite, Mater. Sci. Appl., **1(1)** (2010) 19–24. https://doi.org/10.4236/msa.2010.11004

42. Koops CG, On the dispersion of resistivity and dielectric Constant of some Semiconductors at Audiofrequencies, Phys. Rev., **83** (2002) 121. https://doi.org/10.1103/PhysRev.83.121

43. Zhou SM, Dielectric properties of phase-size-control CdS nanoparticles and conventional powders, Phys. status solidi (a), **200(2)** (2003) 423–428. https://doi.org/10.1002/pssa.200306687

44. Batool SS, Imran Z, Rafiq MA, Hasan MM, et al., Investigation of dielectric relaxation behavior of electrospun titanium dioxide nanofibers using temperature dependent impedance spectroscopy, Ceram. Int., **39(2)** (2013) 1775–1783. https://doi.org/10.1016/j.ceramint.2012.08.024

45. Costa MM, Pires GFM, Terezo AJ, Graça MPF, et al., Impedance and modulus studies of magnetic ceramic oxide $Ba_2Co_2Fe_{12}O_{22}$ (Co_2Y) doped with Bi_2O_3, J. Appl. Phys., **110(3)** (2011) 034107. https://doi.org/10.1063/1.3615935

46. Ahmad M, Rafiq MA, Imran Z, Rasool K, et al., Charge conduction and relaxation in MoS_2 nanoflakes synthesized by simple solid state reaction, J. Appl. Phys., **114(4)** (2013) 043710. https://doi.org/10.1063/1.4816570

47. Liu M, Zhan Q, Li W, Li R, et al., Effect of Zn doping concentration on optical band gap of PbS thin films, J. Alloys Compd., **792** (2019) 1000–1007. https://doi.org/10.1016/j.jallcom.2019.04.117

48. Vankhade D, Kothari A, Chaudhuri TK, Direct-coated Photoconducting nanocrystalline PbS thin Films with tunable Band Gap, J. Electron. Mater., **45** (2016) 2789–2795. https://doi.org/10.1007/s11664-016-4364-1

49. Dey P, Paul J, Bylsma J, Karaiskaj D, et al., Origin of the temperature dependence of the band gap of PbS and PbSe quantum dots, Solid State Commun., **165** (2013) 49–54. https://doi.org/10.1016/j.ssc.2013.04.022

50. Nanda KK, Kruis FE, Fissan H, Acet M, Band-gap tuning of PbS nanoparticles by in-flight sintering of size classified aerosols, J. Appl. Phys., **91(4)** (2002) 2315–2321. https://doi.org/10.1063/1.1431429

51. Jana S, Thapa R, Maity R, Chattopadhyay KK, Optical and dielectric properties of PVA capped nanocrystalline PbS thin films synthesized by chemical bath deposition, Phys. E: Low-Dimens. Syst. Nanostructures, **40(10)** (2008) 3121–3126. https://doi.org/10.1016/j.physe.2008.04.015

52. Shkir M, Chandekar KV, Hossain MM, Palanivel B, et al., Enhanced dielectric and electrical properties of PbS nanostructures facilely synthesized by low-cost chemical route: an effect of Ce doping concentrations, Mater. Chem. Phys., **278** (2022) 125626. https://doi.org/10.1016/j.matchemphys.2021.125626

53. Chandekar KV, Alshahrani T, Ben Gouider Trabelsi A, Alkallas FH, et al., Novel rare earth yttrium doping effect on physical properties of PbS nanostructures: facile synthesis and characterization, J. Mater. Sci., **56** (2021) 4763–4781. https://doi.org/10.1007/s10853-020-05539-w

54. Trabelsi ABG, Alkallas FH, Chandekar KV, Kumar A, et al., Facile low temperature development of Ag-doped PbS nanoparticles for optoelectronic applications, Materials Chemistry and Physics, **297**, (2023) 127299. https://doi.org/10.1016/j.matchemphys.2023.127299

55. Mariappan SM, Hong SJ, Han B, Shkir M, et al., Slow excitonic carrier cooling in Sr-doped PbS nanocrystals for hot carrier devices: an integrated experimental and first-principles approach, Journal of Materials Chemistry C, **10** (2022) 6634–6645. https://doi.org/10.1039/D1TC05921A

56. Shkir M, Chandekar KV, Khan A, El-Toni AM, et al., A facile synthesis of Bi@PbS nanosheets and their key physical properties analysis for optoelectronic technology, Materials Science in Semiconductor Processing, **107** (2020) 104807. https://doi.org/10.1016/j.mssp.2019.104807

57. Shkir M, Khan M T, Ashraf I M, AlFaify S, et al., Rapid microwave-assisted synthesis of Ag-doped PbS nanoparticles for optoelectronic applications, Ceramics International, **45(17)** (2019) 21975–21985. https://doi.org/10.1016/j.ceramint.2019.07.212

58. Shkir M, AlFaify S, A facile low-temperature synthesis of nanosheets assembled PbS microflowers and their structural, morphological, optical, photoluminescence, dielectric and electrical studies, Materials Research Express, **6** (2019) 105013. https://doi.org/10.1088/2053-1591/ab3535

59. Shkir M, Yahia IS, AlFaify S, A facilely one pot low temperature synthesis of novel Pt doped PbS nanopowders and their characterizations for optoelectronic applications, Journal of Molecular Structure, **1192** (2019) 68–75. https://doi.org/10.1016/j.molstruc.2019.04.099

60. Shkir M, Ashraf IM, AlFaify S, Surface area, optical and electrical studies on PbS nanosheets for visible light photo-detector application, Physica Scripta, **94** (2019) 025801. https://doi.org/10.1088/1402-4896/aaf55a

61. Hanif MB, Rauf S, Sultan A, Tayyab Z, et al., Boosting the electrochemical performance of oxygen electrodes via the formation of LSCF-$BaCe_{0.9-x}Mo_xY_{0.1}O_{3-\delta}$ triple conducting composite for solid oxide fuel cells: Part II., Energy, **289** (2024) 129985. https://doi.org/10.1016/j.energy.2023.129985

62. Khan K, Qayyum S, Hanif MB, Rauf S, et al., Design of efficient and durable symmetrical protonic ceramic fuel cells at intermediate temperatures via B-site doping of Ni in $BaCe_{0.56}Zr_{0.2}Ni_{0.04}Y_{0.2}O_{3-\delta}$, Ceramics International, **49(11)** (2023) 16826–16835. https://doi.org/10.1016/j.ceramint.2023.02.043